Crystal growth of clinopyroxene in mafic alkaline magmas

Jin-Sheng Zhou [a,b], Qiang Wang [a,b,c,*], Chang-Ming Xing [d], Lin Ma [a], Lu-Lu Hao [a], Qi-Wei Li [a], Zi-Long Wang [a], Tong-Yu Huang [a]

[a] State Key Laboratory of Isotope Geochemistry, Guangzhou Institute of Geochemistry, Chinese Academy of Sciences, Guangzhou 510640, China
[b] CAS Center for Excellence in Deep Earth Science, Guangzhou, 510640, China
[c] College of Earth and Planetary Sciences, University of Chinese Academy of Sciences, Beijing 100049, China
[d] CAS Key Laboratory of Mineralogy and Metallogeny, Guangzhou Institute of Geochemistry, Guangzhou 510460, China

ARTICLE INFO

ABSTRACT

Recent experimental and natural studies have shown that igneous crystals can start to crystallize through skeletal or dendritic growth, and then backfill progressively to form polyhedral crystal morphologies, in contrast to the traditional tree-ring model of crystal growth. Identifying the growth mechanism of crystal is fundamental to understand crystal growth and associated magmatic processes. Clinopyroxene is an ubiquitous phase in magmatic systems. However, crystallographically controlled zoning patterns (e.g., sector zoning) observed in different studies are diverse or even show opposite trends, which make it challenging to understand the crystal growth mechanisms of clinopyroxene. This study presents a new finding of the contemporary occurrence of both clinopyroxenes with Al-rich and -poor $\{hk0\}$ sectors in the Sailipu alkaline volcanic field in southern Tibet. Based on detailed textural and compositional analyses of a large number of clinopyroxene grains, we suggest a new crystal growth mechanism for clinopyroxene in mafic alkaline magmas. At low degrees of undercooling, all crystal faces grow concurrently, producing equilibrium Si–Mg-rich $\{-111\}$ sectors and disequilibrium Al–Ti-rich $\{hk0\}$ sectors; at high degrees of undercooling, the equilibrium sectors $\{hk0\}$ initially form, which is followed by backfill of disequilibrium Al-rich $\{-111\}$ sectors. Al_2O_3 is a useful indicator of equilibrium, and Al_2O_3-poor sectors, rather than specific crystal faces, are closer to equilibrium. The behavior of other cations is complex and the distribution of their oxide components is variable. Textural observations and the modeling results for P transfer across the crystal–melt diffusive boundary layer show that apatite inclusions in clinopyroxene can indicate rapid crystal growth. These results may contribute to a better understanding of magma storage, ascent and eruption on the basis of clinopyroxene.

© 2021 Elsevier B.V. All rights reserved.

1. Introduction

Igneous crystals are archives of intensive magma parameters and have been widely used to reconstruct the crystallization temperature and pressure of magmatic plumbing systems beneath volcanoes (e.g., Putirka, 2008). One of the recent issues for crystal cargo has focused on the timescales of magmatic processes by diffusion chronometry (e.g., Costa et al., 2020). This approach generally relies on the tree-ring model of crystal growth, whereby material is added sequentially as growth layers to crystals from the core to rim. However, recent experimental work and studies on natural samples have questioned this conventional notion,

and shown that crystallization may start as skeletal or dendritic growth, followed by crystal maturation to form polyhedral morphologies (e.g., Faure et al., 2007; Welsch et al., 2013, 2014, 2016; Ni et al., 2014; Xing et al., 2017; Pontesilli et al., 2019; Shea et al., 2019; Masotta et al., 2020). Thus, under certain circumstances, mineral crystallization does not progress simply from core to rim, and investigations of magmatic plumbing systems based on crystal stratigraphy need to be reconsidered.

Clinopyroxene is an ubiquitous phase in magmatic systems and its crystallization can occur over a wide range of depths, from the mantle to the surface (Putirka, 2017). Clinopyroxene composition is sensitive to pressure, temperature, and magmatic H_2O content and can thus be used to constrain the architecture and dynamics of magmatic plumbing systems (e.g., Putirka, 2008, 2017; Perinelli et al., 2016; Neave and Putirka, 2017; Mollo et al., 2018). In combination with diffusion chronometry, clinopyroxene can be employed to identify magmatic processes with corresponding time
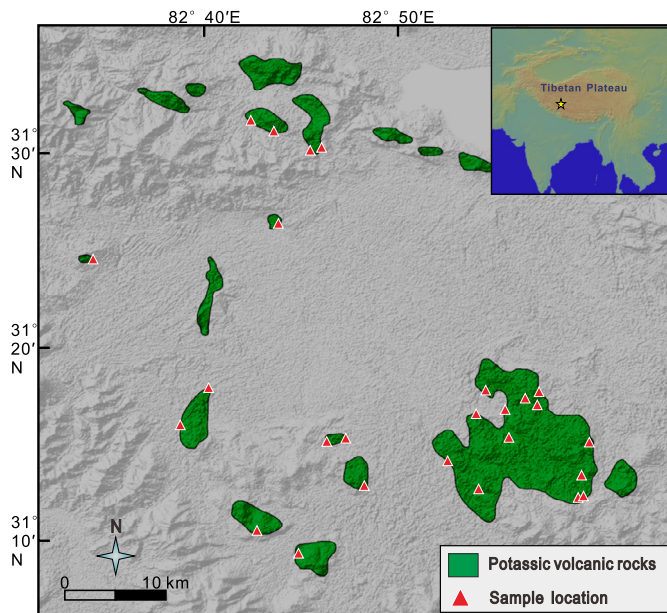
Fig. 1. Simplified geological map showing the distribution of potassic volcanic rocks and sampling locations in the Sailipu volcanic field. The inset map shows the regional-scale geomorphological characteristics and location of the Sailipu volcanic field. The yellow star is Sailipu. (For interpretation of the colors in the figure(s), the reader is referred to the web version of this article.)

information (e.g., Costa et al., 2020). A number of studies, including experimental investigations (e.g., Mollo et al., 2010; Ni et al., 2014; Pontesilli et al., 2019; Masotta et al., 2020) and natural observations (e.g., Hammer et al., 2016; Welsch et al., 2016; Neave et al., 2019; Ubide et al., 2019a,b), indicate that kinetic effects play a critical role during clinopyroxene growth. Sector zoning is a classic texture that results from kinetically controlled crystal growth (e.g., Schwandt and McKay, 2006; Hammer et al., 2016; Welsch et al., 2016; Neave et al., 2019; Ubide et al., 2019a,b). Compositional zoning patterns in different crystallographic directions provide key information about crystallization processes. However, such patterns observed in different studies are complex or even show opposite trends. For example, high contents of cations Al and Ti in the prism sectors {$hk0$} have been observed in many studies, and used to develop the model of interface-controlled cation substitution or element adsorption that is widely thought to explain the formation of sector zoning (e.g., Hollister and Gancarz, 1971; Nakamura, 1973; Dowty, 1976; Shimizu, 1981; Ubide et al., 2019a). However, the opposite zoning pattern (Al-Ti-poor {$hk0$} sectors) also occurs in other magmatic systems such as Hawaii (Hammer et al., 2016; Welsch et al., 2016). This makes it challenging to understand the crystal growth mechanisms of clinopyroxene, as well as to use clinopyroxene to investigate magmatic plumbing systems.

In this study, we investigated potassic, mafic volcanic rocks in the Sailipu volcanic field (Fig. 1), which is located on the southern Tibetan Plateau. The Sailipu volcanic rocks contain abundant clinopyroxene crystals with variable textural types and, in particular, the co-occurrence of clinopyroxenes with Al-rich and -poor {$hk0$} sectors. Thus, the Sailipu volcanic rocks are ideal for investigating the crystal growth mechanisms of clinopyroxene. Based on detailed textural and compositional analysis of a large number of clinopyroxene crystals, we present a new crystal growth model that may reconcile the diverse crystallographic zoning patterns that have been reported previously. Furthermore, our results may allow us to better constrain magma storage, ascent, and eruption when using clinopyroxene crystals as an archive of these processes.

2. Background and samples

2.1. Crystallization kinetics of clinopyroxene in mafic alkaline magmas

The formation of an igneous crystal involves a series of steps. The thermodynamic driving force for crystallization is negative at superliquidus temperatures. A certain degree of undercooling is required for crystal nucleation and growth. Thermodynamic effective undercooling (ΔT) is the difference between the liquidus temperature and system temperature (Kirkpatrick et al., 1981). Two common factors that can result in effective undercooling in natural systems are cooling and degassing (Hammer, 2008; Mollo and Hammer, 2017), which decrease the system temperature or increase the liquidus temperature, respectively. In a state of undercooling, the excess free energy drives crystallizing components to form a nucleus on which crystal growth can occur, assuming that no crystal nuclei are present. Both crystal nucleation and growth rates increase rapidly to maximums and then decrease relatively slowly with increasing ΔT, but the nucleation maximum generally occurs at higher degrees of undercooling (e.g., Mollo and Hammer, 2017). Once a nucleus has formed, the addition of elements from the surrounding melt sustains crystal growth. The growth rate is affected by several factors, including diffusion- and interface-controlled growth, which are governed by the relationship between the component mobility in the melt and attachment rate on the crystal surface (Hammer, 2008). The rate of crystal growth is also a function of ΔT. At small degrees of undercooling, crystals grow near chemical and textural equilibrium and growth is interface-controlled, resulting in the formation of polyhedral crystals (Herring, 1951). In contrast, rapid crystal growth at high degrees of undercooling increases the likelihood of departure from textural equilibrium, and forms crystals with disequilibrium morphologies, such as skeletal and dendritic forms (e.g., Faure et al., 2007; Ni et al., 2014; Pontesilli et al., 2019; Masotta et al., 2020).

Clinopyroxene is an excellent mineral for investigating the mechanisms of rapid crystal growth, because the degree of undercooling has a considerable effect on clinopyroxene composition and texture (e.g., Pontesilli et al., 2019; Masotta et al., 2020), particularly in mafic alkaline magmas (e.g., Hollister and Gancarz, 1971; Downes, 1974; Leung, 1974; Shimizu, 1981). As a classic texture resulting from rapid crystal growth, sector zoning within clinopyroxene was often ignored probably because of difficulty in observing them (Schwandt and McKay, 2006). However, in recent years, an increasing number of studies have revisited the petrological significance of sector zoning (e.g., Hammer et al., 2016; Welsch et al., 2016; Neave et al., 2019; Ubide et al., 2019a,b). Within a sector-zoned crystal, different faces have varying growth rates and compositions, which produces pyramid-shaped domains that extend outward from the crystal center (Fig. 2). This poses a particular challenge for petrological studies, because different sectors may grow from the same melt under the same conditions (Ubide et al., 2019a). Experimental studies (e.g., Kouchi et al., 1983; Masotta et al., 2020) have shown that at relatively low degrees of undercooling ($\Delta T = 13$–$25\,°C$), the hourglass sectors such as {-111} are Si- and Mg-rich, and the prism sectors {100}, {110}, and {010} are Al- and Ti-rich. In contrast, at higher degrees of undercooling, the crystal interiors show irregular contact between two domains, with the zoning pattern of Al-Ti-rich dendrites surrounded by Si-Mg-rich overgrowths (Masotta et al., 2020). Several mechanisms have been proposed to explain the origin of sector zoning, principally based on crystallographic or diffusion controls (e.g., Schwandt and McKay, 2006; Welsch et al., 2016; Ubide et al., 2019a).
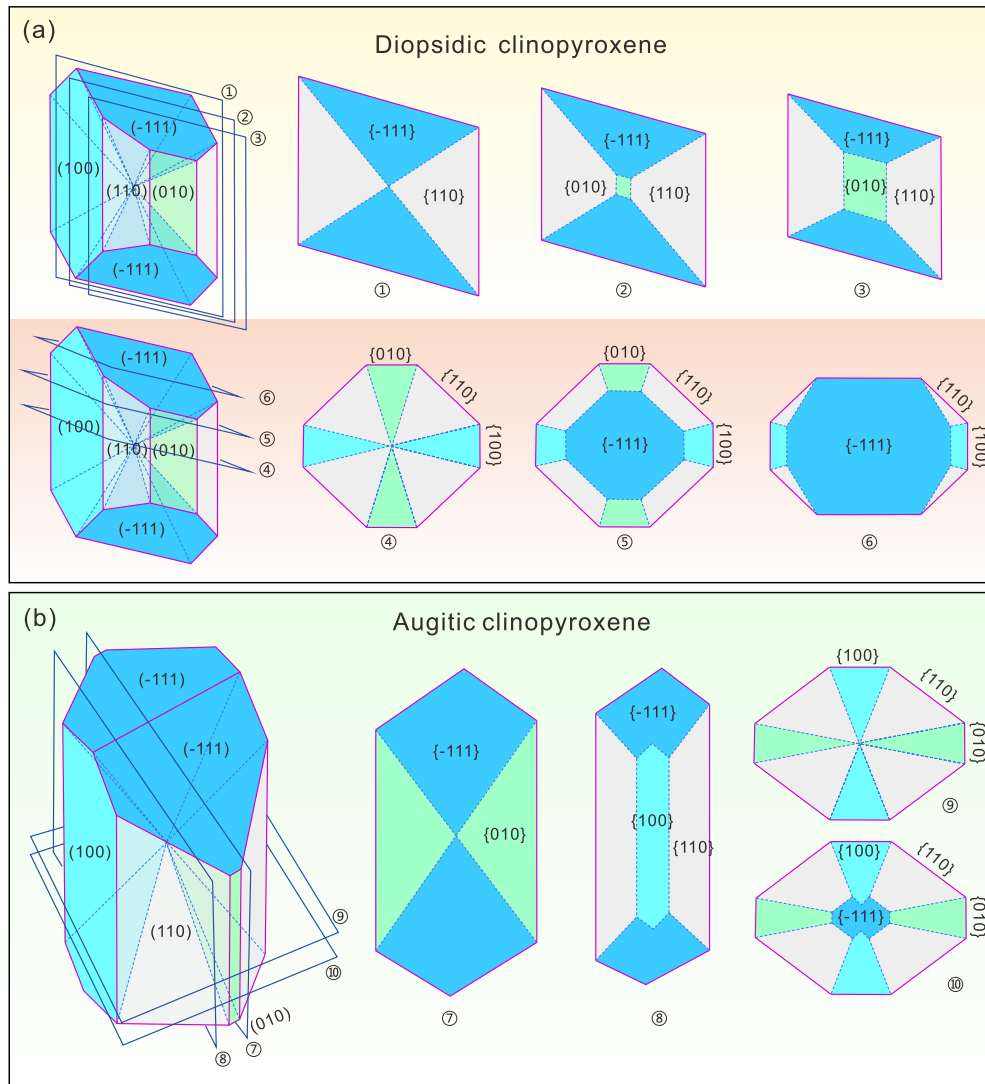
Fig. 2. Crystal model of sector-zoned diopsidic (Welsch et al., 2016) and augitic clinopyroxenes (Ubide et al., 2019a). Four sector families, which are the prism sectors {100}, {110}, and {010} parallel to the c-axis, and the hourglass sector {−111} along the c-axis, are shown in different colors. In general, sectors {100}, {110}, and {010} are commonly referred to as {$hk0$} sectors. Several ideal cuts of the crystal in different orientations are also shown. Some cuts perpendicular to the c-axis have similar zoning patterns as concentric zoning (cuts ⑤ and ⑩).

2.2. Sailipu volcanic field and samples

The Sailipu volcanic field is located on the southern Tibetan Plateau (Fig. 1), which comprises several microcontinent terranes and is presently experiencing tectonism due to multiple subduction and collisional processes. The Lhasa Terrane is located in the southern Tibetan Plateau. The southern Lhasa Terrane is bordered by the youngest suture zone in the Tibetan Plateau; i.e., the Indus–Tsangpo suture zone, which closed at Paleocene when collision began between the Asian and Indian continents. There are >13 mafic alkaline volcanic fields in the Lhasa Terrane (Guo et al., 2015). Most of these erupted at ca. 25 to 8 Ma, and are distributed along N–S-trending rifts (Zhao et al., 2009; Liu et al., 2014; Guo et al., 2015; Guo and Wilson, 2019). The Sailipu alkaline volcanic field contains numerous mafic to intermediate volcanic cones (Fig. 1). Zircon U–Pb and ^{40}Ar/^{39}Ar dating has shown that volcanism in the Sailipu field began at 18.48 ± 0.34 Ma and ceased at 15.47 ± 0.30 Ma (Guo and Wilson, 2019). The volcanic rocks are phonotephrites, basaltic trachyandesites, and trachyandesites. In this study, a large number of clinopyroxene crystals (including phenocrysts and mi-

crolites) from five phonotephrite, six basaltic trachyandesite, and ten trachyandesite samples were investigated and analyzed.

3. Analytical methods

Mineral major element contents were analyzed using a JEOL JXA 8230 electron probe micro-analyzer (EPMA), using a 15 kV accelerating voltage, 20 nA beam current, and 1 µm beam diameter, in the Key Laboratory of Mineralogy and Metallogeny (KLMM) of the Guangzhou Institute of Geochemistry, Chinese Academy of Sciences (GIG–CAS), Guangzhou, China, and with a JEOL JXA 8100 Superprobe, using a 15 kV accelerating voltage, 20 nA beam current, and 2 µm beam diameter, at the State Key Laboratory of Isotope Geochemistry (SKLaBIG), GIG–CAS. ZAF (Z: atomic number; A: absorption; F: fluorescence) corrections were applied to reduce the results. The standards used include Cr-diopside (Si and Ca), magnetite (Fe), olivine (Mg), almandine garnet (Al), rutile (Ti), rhodonite (Mn), Cr_2O_3 (Cr), and albite (Na). The 1σ precision was $<\pm3\%$.

High-resolution, two-dimensional, elemental X-ray mapping was performed using a JEOL JXA-8230 EPMA in the KLMM, GIG–

CAS, with an accelerating voltage of 20 kV, a probe current of 200 nA, and a beam size of 1 μm. The dwell time was 100 ms for each point. Al Kα and Na Kα were analyzed with a TAP crystal. Ti Kα was analyzed with a LIF crystal. Cr Kα was analyzed with a LIFH crystal. P Kα was analyzed with a PETH crystal.

4. Results

4.1. Petrography

Textural features of the clinopyroxene crystals are shown in Figs. 3–4 and Supplementary Figs. S1–S2, and described in Supplementary Table S1. In this study, we used the terms "phenocrysts" and "microcrysts" to describe the relatively large and small crystals, respectively, in one sample. However, the sizes of phenocrysts and microcrysts vary among different samples. The phenocrysts occur as single crystals (Fig. 3a), growth twins (Fig. 4a), or crystal aggregates (Fig. 3b, g). In terms of grain size and texture, the clinopyroxene crystals can be subdivided into five populations: polyhedral phenocrysts without spongy domains and sector zoning (hereafter referred to as polyhedral phenocrysts; Fig. 3a), spongy phenocrysts (Fig. 3h), sector-zoned phenocrysts (Fig. 3g; Fig. 4; Supplementary Fig. S1), polyhedral microcrysts (Supplementary Fig. S2d), and spongy microcrysts (Fig. 3f). Most phenocrysts have polyhedral external morphologies (Fig. 3), and crystallographically aligned subcrystals (i.e., buds; Welsch et al., 2016) are developed around some crystals (Figs. 3c and 4a). {100} twins are common (Fig. 4a), as observed in other studies (e.g., Welsch et al., 2016). The crystal aggregates have diverse structures, including radial structures (Fig. 3b) and groups of parallel crystals. Many crystals, including phenocrysts and microcrysts, contain internal cavities, which are either empty (Fig. 3e) or filled with highly evolved glass (anomalously low CaO and MgO and high Al$_2$O$_3$ contents; Fig. 3h; Supplementary Table S4), groundmass material (Fig. 3d), or other minerals (Fig. 3f). In thin-section, some internal cavities are observed to be connected with the groundmass (Fig. 3d, e), whereas others appear to be closed (Fig. 3f, h). Glass within the internal cavities occasionally encloses gas bubbles (Fig. 3h). In some cases, clinopyroxene compositions near the internal cavities are heterogeneous, and have an irregular, porous, spongy domain (Fig. 3f, h). Crystal zoning can be observed in back-scattered electron (BSE) images. Oscillatory zoning is the most common type of zoning (Fig. 3a, b, e), and normal and reverse zoning also occurs (Fig. 3f, i). Phenocrysts with sector zoning are dominantly present in samples that contain clinopyroxene crystals with spongy domains (Fig. 4). Some sector-zoned crystals have outer rims, which form a pattern of complex zoning (Fig. 4b).

Notably, apatite inclusions are considerably abundant in most clinopyroxene crystals (Fig. 3–4; Supplementary Fig. 1–2). In some sector-zoned crystals, the prism sectors {hk0} contain more apatite inclusions than the hourglass sector {−111} (e.g., Fig. 3g as well as crystal #5 in Supplementary Fig. S1). Some phenocrysts and microcrysts have cores with abundant apatite inclusions, whereas their rims are relatively inclusion-free (Fig. 3f; Supplementary Fig. S2c). In contrast, some other microcrysts contain relatively inclusion-free cores, but inclusion-rich rims (Supplementary Fig. S2d).

4.2. Microanalytical results

Major element analyses clinopyroxene and the glass filled in internal cavities of clinopyroxene are presented in the Supplementary Tables S2–S4. All clinopyroxene major element compositions are shown in Supplementary Fig. S3, and sector-zoned clinopyroxene compositions are illustrated in Fig. 5. The compositions of polyhedral phenocrysts are highly variable, and most of them are diopsidic or augitic (Wo$_{39–52}$En$_{35–51}$Fs$_{4–18}$) with Mg# = 0.63–0.92

(Supplementary Fig. S3). Most of the polyhedral phenocrysts have relatively high SiO$_2$ and CaO contents, but low TiO$_2$, Al$_2$O$_3$, FeO$_{total}$, and Na$_2$O contents (Supplementary Fig. S3). The spongy phenocrysts are also diopsidic to augitic (Wo$_{38–50}$En$_{42–51}$Fs$_{6–17}$), with Mg# = 0.71–0.85 (Supplementary Fig. S3). These phenocrysts are relatively rich in TiO$_2$, Al$_2$O$_3$, FeO$_{total}$, and Na$_2$O, and poor in SiO$_2$ and CaO (Supplementary Fig. S3). Most sector-zoned phenocrysts (Wo$_{33–53}$En$_{36–54}$Fs$_{4–15}$; Mg# = 0.75–0.91) have similar compositions to the spongy phenocrysts (Supplementary Fig. S3). The polyhedral microcryst compositions (Wo$_{39–53}$En$_{43–51}$Fs$_{3–13}$; Mg# = 0.78–0.92) overlap those of the polyhedral phenocrysts (Supplementary Fig. S3).

Ten sector-zoned phenocrysts were investigated in this study (Supplementary Fig. S1). Crystallographic orientations were determined by comparison with theoretical cuts across crystal models of diopsidic (Welsch et al., 2016) and augitic clinopyroxenes (Ubide et al., 2019a). The two sector families, which are the prism sectors {hk0} (including sectors {100}, {110}, and {010}) parallel to the c-axis, and hourglass sector {−111} along the c-axis, are compositionally distinct (Fig. 5). In general, most {−111} sectors have relatively higher SiO$_2$ and MgO contents, but lower TiO$_2$, Al$_2$O$_3$, Na$_2$O, and Cr$_2$O$_3$ contents than the {hk0} sectors (Fig. 5). However, there is an exception (Fig. 3g as well as crystal #5 in Supplementary Fig. S1) where the {−111} sectors are enriched in Al$_2$O$_3$, Na$_2$O and Cr$_2$O$_3$, but depleted in TiO$_2$ (Fig. 5). In addition, one sector-zoned phenocryst (crystal #10 in Supplementary Fig. S1) exhibits clear zonation of Al within the interior of a {−111} sector (Fig. 4b).

5. Discussion

5.1. Clinopyroxene-melt equilibrium and geothermobarometry

Clinopyroxene–melt thermobarometry is a powerful tool for reconstructing pre-eruptive magmatic processes, particularly in determining the depths where magmas are stored (e.g., Hammer et al., 2016; Putirka, 2017). A series of clinopyroxene-based calibrations has been developed (Putirka, 2008; Perinelli et al., 2016; Neave and Putirka, 2017; Mollo et al., 2018) and widely used in petrological studies (e.g., Zhou et al., 2020). It is necessary to assess whether chemical equilibrium existed before undertaking thermodynamic calibrations. The Fe–Mg exchange coefficient (K_D(Fe–Mg)$^{cpx–melt}$) is an important test for equilibrium between mafic minerals (including clinopyroxene) and melt (e.g., Putirka, 2008). This coefficient is temperature-dependent for clinopyroxene: $\ln K_D$(Fe–Mg)$_{cpx–melt}$ = $-0.107 - 1719/T$ (Putirka, 2008), where T is temperature. However, dynamic crystallization experiments have demonstrated that clinopyroxene compositions are also controlled by the degree of undercooling (Mollo et al., 2010, 2013; Mollo and Hammer, 2017; Neave et al., 2019). For example, Al and Na contents and Mg# values of clinopyroxene increase, but Mg and Ca contents decrease, with increasing cooling rate (Mollo et al., 2010, 2013). In detail, the Fe–Mg exchange coefficient of clinopyroxene increases and then remains constant with increasing cooling rate (Mollo et al., 2013; Mollo and Hammer, 2017), suggesting that assessing clinopyroxene–melt equilibrium with K_D(Fe–Mg)$^{cpx–melt}$ values may be inappropriate if clinopyroxene growth occurred at large degrees of undercooling. Mollo et al. (2013) suggested that a comparison between predicted and measured components (such as enstatite–ferrosilite [EnFs] and diopside–hedenbergite [DiHd] components) in clinopyroxene is a more robust test for equilibrium.

Most of the groundmass surrounding the clinopyroxenes is highly crystalline (Fig. 3), thus precluding the determination of melt compositions by analyzing glasses. Whole-rock compositions are an alternative option for determining the equilibrium melt composition. Using the whole-rock compositions of the host, the
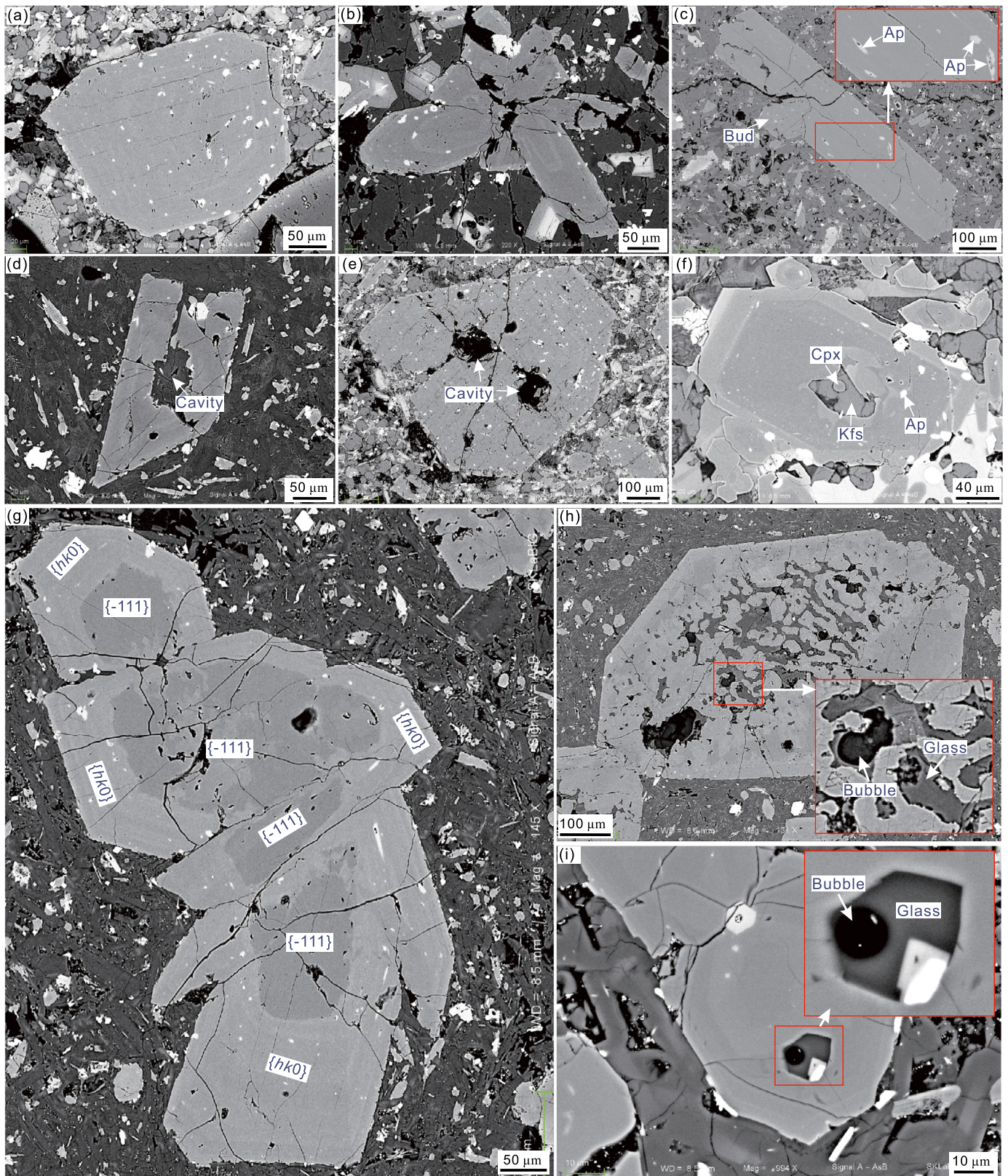
Fig. 3. Textural characteristics of representative clinopyroxene crystals. (a) Single phenocryst with polyhedral external morphology. (b) Crystal aggregate with radial structure. (c) Single phenocryst with crystallographically aligned sub-crystals (i.e., buds). (d) Phenocryst with an internal cavity that is connected to the groundmass. (e) Phenocryst with empty internal cavities. (f) Normally zoned microcryst with an internal cavity that is filled by K-feldspar. (g) Crystal aggregate with sector-zoned crystals. It is noteworthy that sector-zoning in these crystals is similar to concentric zoning in which the inner domains represent inherited cores. However, phenocrysts with inherited cores commonly occur as an isolated crystal, in contrast, such a group of crystals with an identical zoning pattern should be crystallographically controlled. In addition, clinopyroxene phenocrysts without apatite inclusions are extremely rare in the Sailipu magmatic system, but no apatite inclusions can be found in the inner domains of these crystals. (h) Typical spongy phenocryst. Glasses within the internal cavities are highly evolved melts (anomalously low CaO and MgO but high Al_2O_3 contents; Supplementary Table S4) and contain gas bubbles. (i) Reversely zoned microcryst with a melt inclusion.
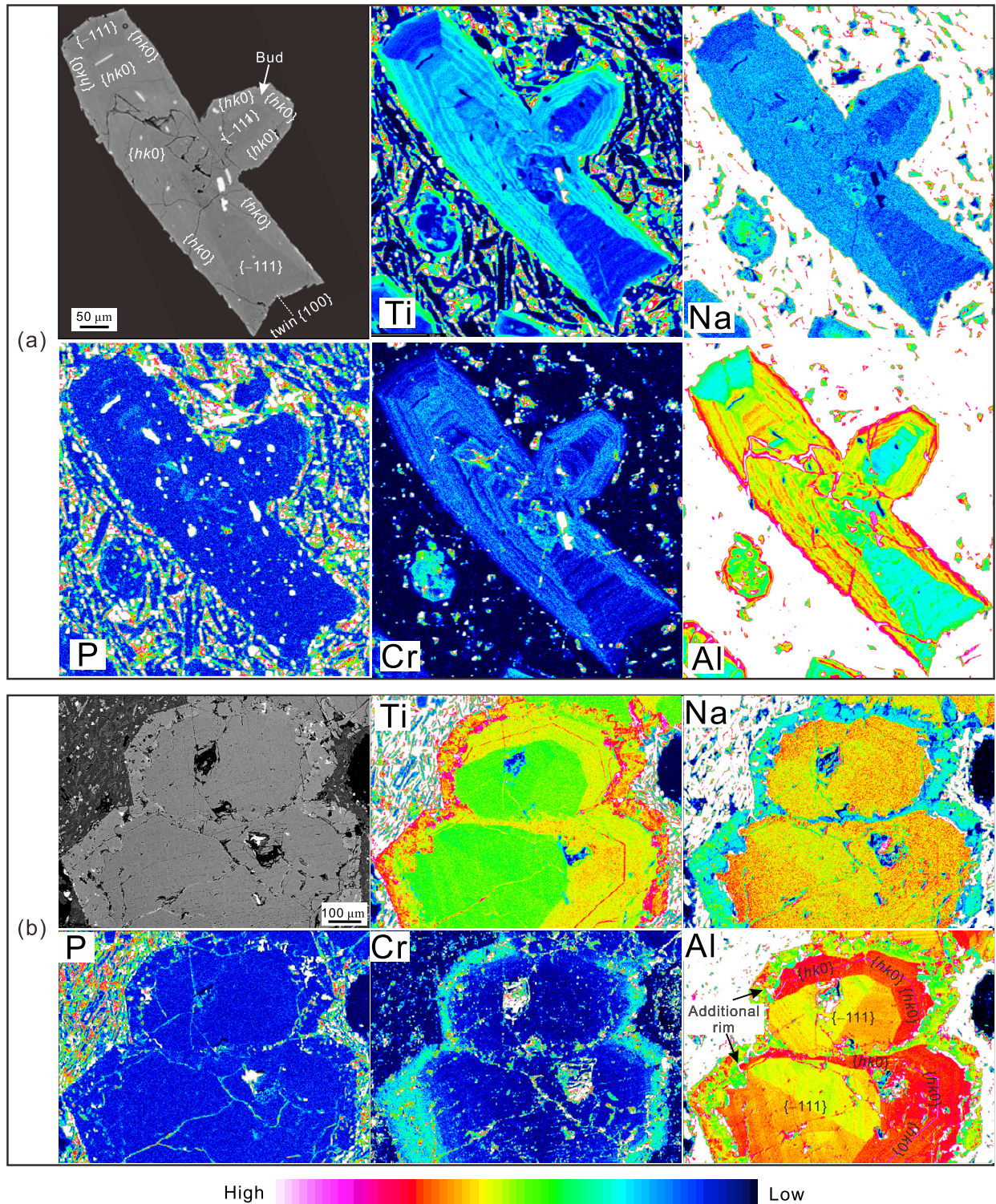
Fig. 4. Back-scattered electron images and EPMA elemental X-ray maps of two sector-zoned clinopyroxene phenocrysts. (a) Clinopyroxene {100} twins with sector zoning. The {−111} sectors have lower Ti, Na, Cr, and Al contents than the {hk0} sectors. (b) Clinopyroxene aggregate with sector zoning. The sector-zoned cores have rims. Interestingly, the sector-zoned cores exhibit clear zonation of Al within the interior of the {−111} sectors.

difference between the predicted and measured DiHd and EnFs components is shown in Fig. 6a–b. In addition, other equilibrium tests, including a comparison of predicted and measured partition coefficients for Na (D_{Na}) and Ti (D_{Ti}) and the Fe–Mg exchange coefficient are also shown in Fig. 6c–e. In general, clinopyroxene compositions from crystal-poor samples are within 1 standard error of estimate (SEE) of the predicted values, and clinopyroxene compo-

sitions from crystal-rich samples are within 2SEE of the predicted values (Fig. 6a–b). If values of ΔDiHd (i.e., the difference between Di and Hd) of ≤0.1 are considered indicative of equilibrium, as recommended by Mollo et al. (2018), the majority of the Sailipu clinopyroxenes are in equilibrium with their whole-rock compositions. The equilibrium relationships are not perfect in the comparisons of predicted and measured D_{Na}, D_{Ti}, and K_D(Fe–Mg) values
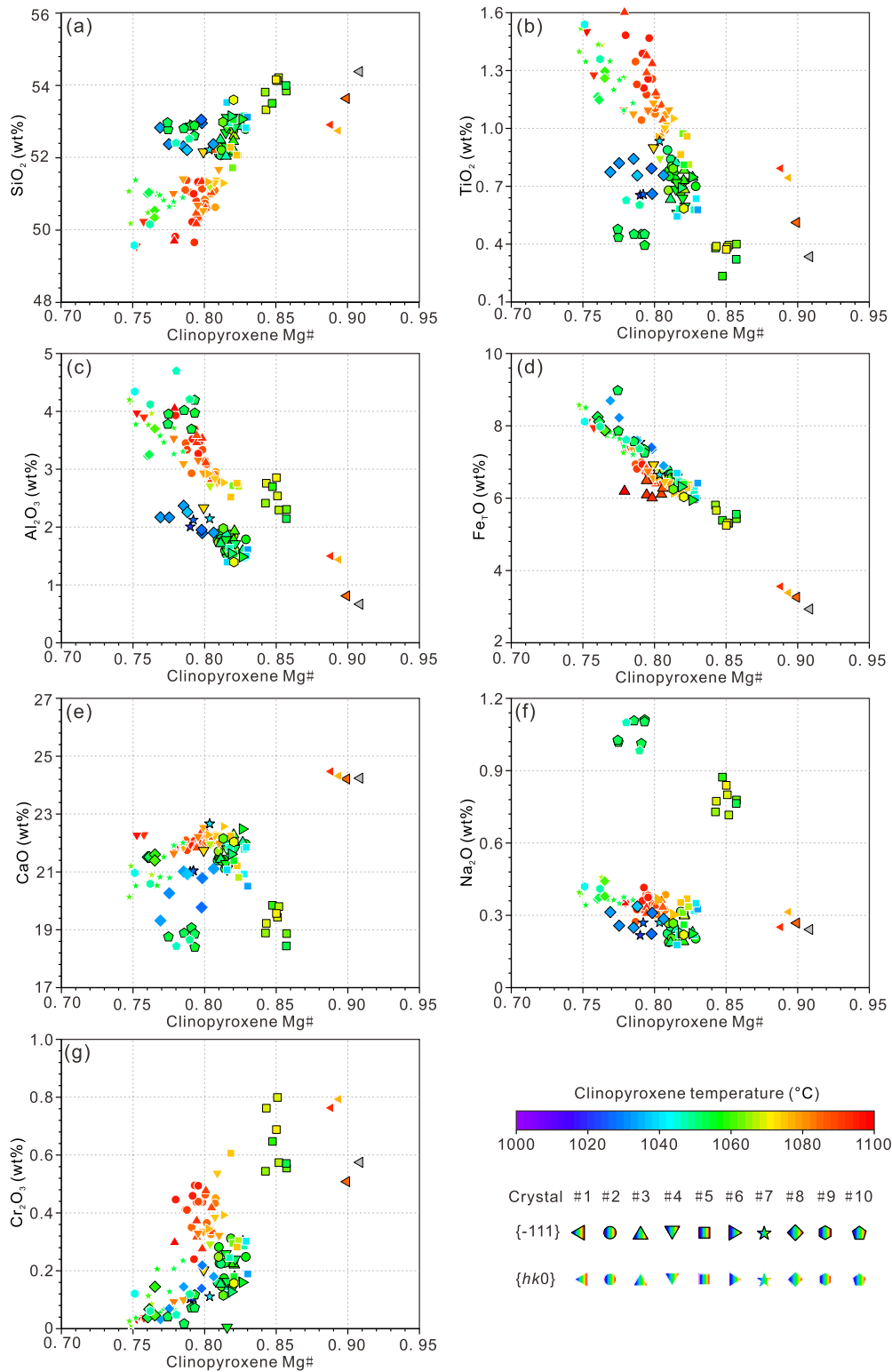
Fig. 5. Comparison of major element contents between the {−111} and {*hk*0} sectors. Different sector-zoned crystals are shown as different symbols. Colors of the symbols correspond to crystallization temperatures that were obtained with the calibration of Mollo et al. (2018). The crystal numbers are the same as in Supplementary Fig. S1.

(Fig. 6c–e). However, the comparison between predicted and observed DiHd and EnFs components in clinopyroxene is a more robust test than the other methods for assessing clinopyroxene–melt equilibria (Mollo et al., 2013). Thermobarometric and hygrometric calculations were undertaken on clinopyroxene–melt pairs using the algorithms of Mollo et al. (2018), which are specifically ap-

plicable to mafic alkaline magmas. The results are shown in Fig. 7, which highlights the wide range in crystallization conditions of the Sailipu clinopyroxenes. In general, the polyhedral phenocrysts and microcrysts crystallized at high pressures (>∼500 MPa), whereas most sector-zoned and spongy phenocrysts formed at relatively low pressures (<∼500 MPa). Crystallization temperatures of the
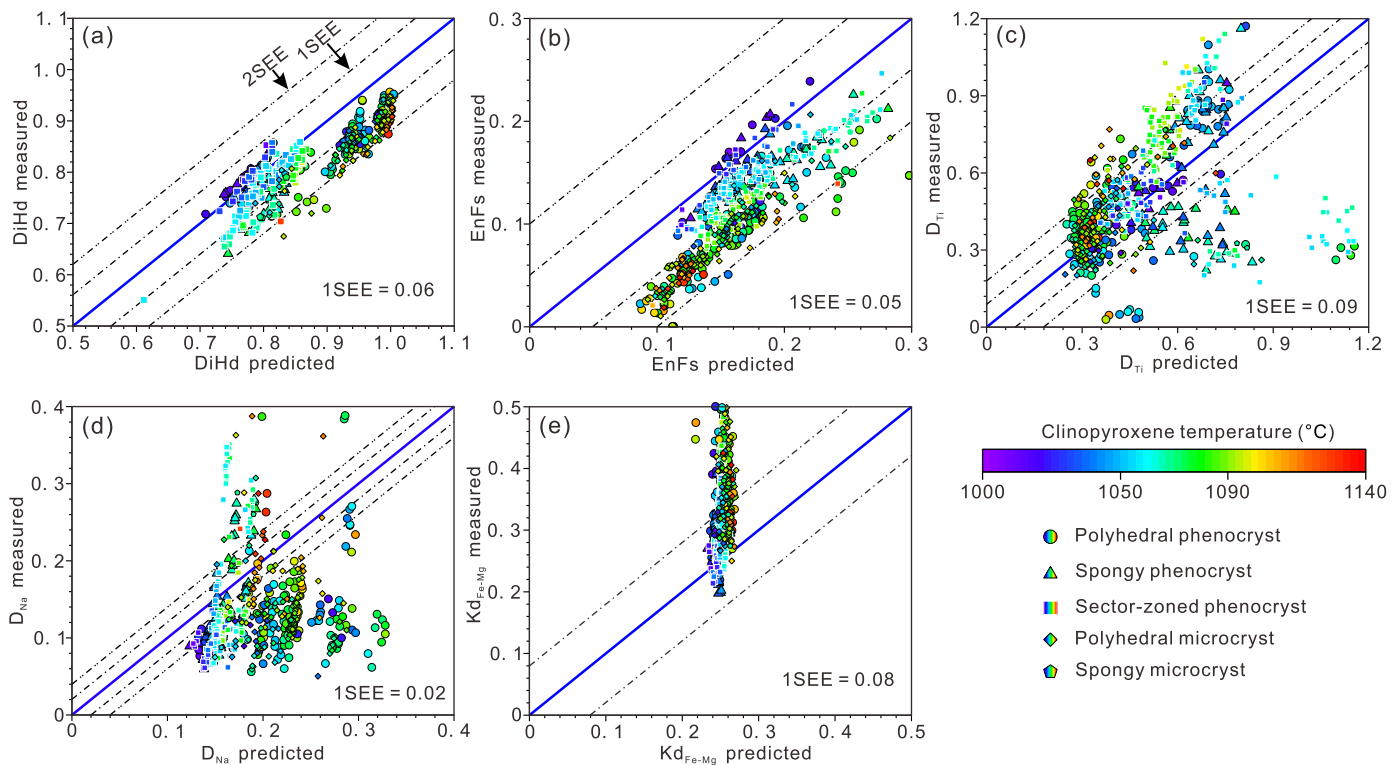
Fig. 6. Comparison of predicted versus measured DiHd, EnFs, D_{Na}, D_{Ti}, and K_D(Fe–Mg) of five crystal types, including polyhedral phenocrysts, spongy phenocrysts, sector-zoned phenocrysts, polyhedral microcrysts, and spongy microcrysts. Observed DiHd and EnFs components were calculated following Putirka (1996), and predicted DiHd and EnFs components were calculated using the equations of Mollo et al. (2013). Predicted D_{Na}, D_{Ti}, and K_D(Fe–Mg) values were calculated using the equations of Blundy et al. (1995), Mollo et al. (2018), and Putirka (2008), respectively. Lines that show a 1:1 relationship between the observed and predicted values are in blue. Model uncertainties (1SEE and 2SEE) are shown as dashed black lines. Colors of the symbols correspond to crystallization temperatures.

Sailipu clinopyroxenes vary from 1000 to 1140 °C. The Sailipu clinopyroxenes record magmatic H_2O contents of ∼1–∼3 wt.% (Fig. 7c, f, i, l).

Disequilibrium crystal growth is a challenge for applying thermodynamic calibrations, because compositionally heterogeneous domains within an individual crystal might have crystallized from the same melt at similar $P–T$ conditions, especially for clinopyroxene, where disequilibrium textures (e.g., sector zoning) have formed because of the extent of undercooling (e.g., Welsch et al., 2016; Ubide et al., 2019a). Within the sector-zoned clinopyroxenes, there is an apparent difference in the compositions of the different crystallographic forms. However, which form is closer to equilibrium remains unclear. One group of studies has suggested that the prism sectors {hk0} record equilibrium compositions (e.g., Hammer et al., 2016; Welsch et al., 2016; Neave et al., 2019), whereas another group has proposed that the hourglass sectors {−111} are much closer to equilibrium (e.g., Ubide et al., 2019a). To assess the degree of equilibrium between different crystallographic forms of the Sailipu clinopyroxenes and their host melts, we compared the predicted and measured DiHd and EnFs components (Fig. 8a–b), as well as the K_D(Fe–Mg) values (Fig. 8c). Whole-rock compositions were assumed as the compositions of host melts, because clinopyroxenes are the major mafic phase in the samples that contain sector-zoned crystals and they crystallized during the early stages of crystallization. Based on the DiHd and EnFs components, different sectors of most of the sector-zoned clinopyroxenes have components that are within or near 1SEE of predicted values and exhibit "equilibrium" compositions, except for crystals #1 and #5. In terms of the commonly used tests for equilibrium, it is difficult to identify the data from disequilibrium sectors. However, the {−111} sectors in most sector-zoned crystals are closer to the 1:1 line in the DiHd and EnFs equilibrium models (Fig. 8a–b), as well as in the K_D(Fe–Mg) equilibrium model (Fig. 8c). Thus, the

low-temperature {−111} sectors likely record the true equilibrium compositions of most Sailipu sector-zoned clinopyroxenes. Compositional differences amongst the sectors result in variable $P–T$ estimates from an individual crystal. Apart from crystals #1 and #5, $P–T$ estimated from {hk0} sectors are 10–36 °C and 39–169 MPa higher than those obtained from {−111} sectors, respectively (Fig. 8d). However, for crystal #5, the {hk0} sectors are closer to equilibrium than the {−111} sectors (Fig. 8a), indicating that the equilibrium compositions do not always correspond to {−111} sectors. In general, the Al_2O_3-poor sectors preferentially record near-equilibrium compositions (Figs. 5 and 8).

5.2. The origin of sector zoning

Clinopyroxene is a classic example of mineral sector zoning, which was identified several decades ago (e.g., Hollister and Gancarz, 1971; Downes, 1974; Leung, 1974; Shimizu, 1981; Watson and Liang, 1995). Varieties of mechanisms have been proposed for the formation of sector zoning, although which of these is correct remains unclear. The possible mechanisms include: (1) interface-controlled cation substitution or element adsorption (e.g., Hollister and Gancarz, 1971; Nakamura, 1973; Dowty, 1976; Shimizu, 1981; Neave et al., 2019; Ubide et al., 2019a); (2) the interplay of crystallographic controls and diffusion limitations (e.g., Downes, 1974; Leung, 1974; Watson and Liang, 1995; Lofgren et al., 2006; Schwandt and McKay, 2006); or (3) initially dendritic growth of {−111} sectors followed by backfill on {hk0} sectors (Welsch et al., 2016). Irrespective of these possibilities, there is no doubt that sector zoning forms during crystal growth and will not be modified by subsequent volume diffusion, as evidenced by experimental observations that sector-zoned cores remain stable, even if slowly grown and compositionally uniform rims form (Schwandt and McKay, 2006).
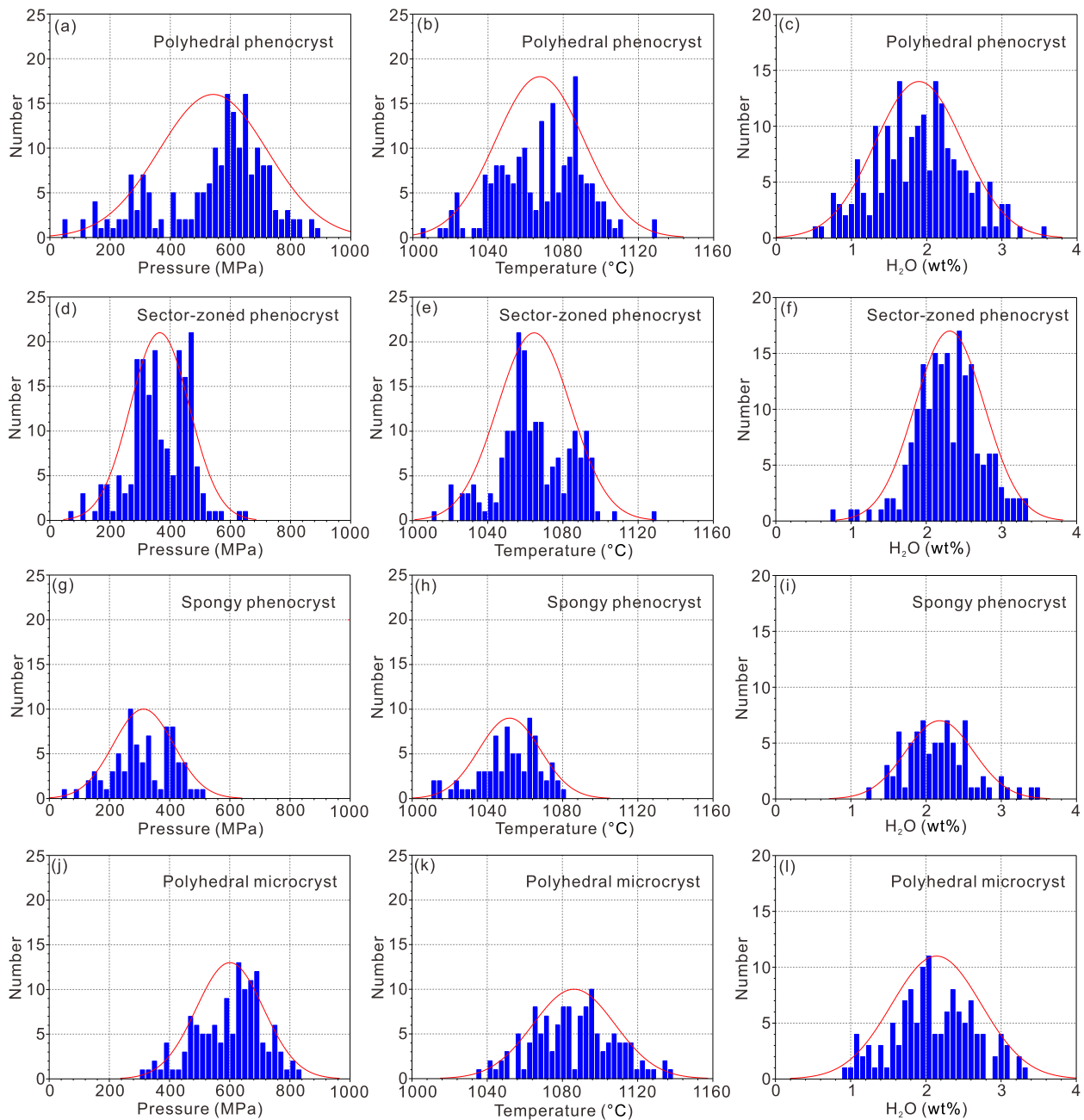
Fig. 7. Calculated P-T-H_2O results of the Sailipu clinopyroxenes with different texture types, using the equations of Mollo et al. (2018).

Major and trace element differences between the sectors provide important information about the formation of sector zoning. It is challenging to determine the mechanism responsible for formation of sector zoning, given the diverse or even opposite compositional zoning patterns observed in different studies (e.g., Welsch et al., 2016; Ubide et al., 2019a). For the Sailipu sector-zoned clinopyroxenes, most {−111} sectors have higher concentrations of Si and Mg, but lower concentrations of Ti, Al, Na, and Cr than the {hk0} sectors (Fig. 5). This observation and those of previous studies (Neave et al., 2019; Ubide et al., 2019a) suggest that major cation exchange between the {−111} and {hk0} sectors of the clinopyroxenes is $[Si^{4+} + Mg^{2+} + Fe^{2+}]_{-111} \leftrightarrow [Al^{3+} + Ti^{4+} + Fe^{3+} + Na^+ + Cr^{3+}]_{hk0}$. However, Al-rich {−111} sectors also exist (Fig. 3g). Simply assuming that the hourglass {−111} sectors are always enriched or depleted in impurity cations (e.g., Al and Ti) is thus inappropriate. The experimental data of Kouchi et al. (1983) showed

that Al and Ti are enriched in the {hk0} sectors at $\Delta T = 13$–$25\,°C$, but are enriched in the {−111} sectors at $\Delta T = 45\,°C$, suggesting a transition in the incorporation of elements from low to high degrees of undercooling. This experimental result is consistent with the Sailipu clinopyroxene crystals, in which the Al-rich {−111} sectors occur as crystal aggregates where the sub-crystals have identical zoning patterns (Fig. 3g). It suggests that they were formed from a single nucleation event at very high supersaturation (i.e., high ΔT; Welsch et al., 2013, 2016). It should be noted that Al–Ti-poor {−111} sectors are more common in natural samples, such as in this (Fig. 5) and previous studies (e.g., Downes, 1974; Leung, 1974; Shimizu, 1981; Schwandt and McKay, 2006; Neave et al., 2019; Ubide et al., 2019a,b).

By integrating the observations of this study with earlier models and experimental results (e.g., Kouchi et al., 1983; Ni et al., 2014; Giuliani et al., 2020; Masotta et al., 2020), we propose two
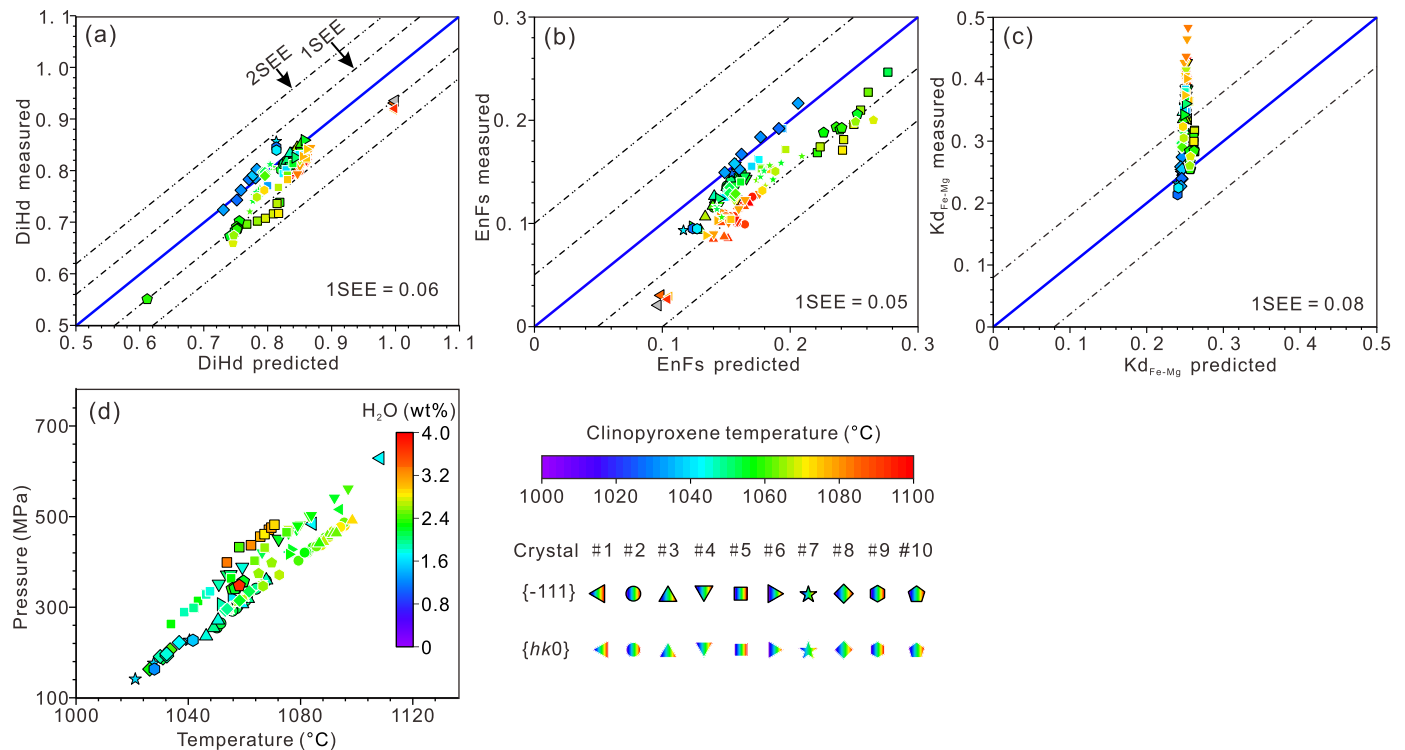
Fig. 8. (a)–(c) Comparison of predicted vs. measured DiHd, EnFs, and K_D(Fe–Mg) values for the sector-zoned clinopyroxenes. (d) Calculated temperatures, pressures, and H_2O contents of the sector-zoned clinopyroxenes obtained using the models of Mollo et al. (2018). Colors of the symbols correspond to temperatures in (a)–(c) and H_2O contents in (d).

different scenarios for the origin of sector-zoned clinopyroxenes (Fig. 9). The first scenario occurs at low degrees of undercooling ($\Delta T < 45\,°C$), when all crystal faces grow concurrently, as evidenced by the concentric zones that cut through the sector zone boundaries (Fig. 4a; crystals #7 and #8 in Supplementary Fig. S1). In this case, the growth rates of the {−111} sectors are faster than those of the {$hk0$} sectors. Sector-zoned clinopyroxenes formed by this process generally have Si–Mg-rich {−111} and Al–Ti-rich {$hk0$} sectors, and the {−111} sectors are closer to equilibrium (Fig. 8a–b). The compositional zoning pattern may be controlled by preferential adsorption of cations into specific crystal faces (e.g., Nakamura, 1973; Dowty, 1976; Shimizu, 1981), charge-compensating coupled substitution (e.g., Hollister and Gancarz, 1971; Ubide et al., 2019a), or a combination of crystallographic control and diffusion limitations (e.g., Downes, 1974; Leung, 1974; Lofgren et al., 2006; Schwandt and McKay, 2006). The second scenario corresponds to high degrees of undercooling ($\Delta T > 45\,°C$), where the prism {$hk0$} sectors initially form, which is followed by backfill of Al-rich {−111} sectors (Fig. 9); in this case, early dendritic growth and ripening at high ΔT generate hopper crystals (i.e., {$hk0$} sectors), which have been observed in experimental run products (e.g., Ni et al., 2014). The irregular, bright, Si- and Mg-poor but Ti-rich domains within the {−111} sectors may represent the early formed dendrites (Fig. 3g), consistent with the experimental work by Pontesilli et al. (2019) and Masotta et al. (2020). These hopper crystals have V-shaped cavities (i.e., {−111} sectors), in which there is a crystal–melt boundary layer with high Al contents, which has been observed experimentally (Masotta et al., 2020). As such, the crystal domains formed in V-shaped cavities ({−111} sectors) are characterized by high Al_2O_3 contents. The behavior of the other cations is complex and may be controlled by several factors, such as differences in element contents between crystal and melt, cation diffusivity in the melt, and charge-compensating coupled substitution, which leads to variable distribution of elements between the {−111} and {$hk0$} sectors.

For example, Si diffuses very slowly in silicate melt (Zhang et al., 2010) and will be concentrated in the boundary layer, if its content in the clinopyroxene is lower than in the melt. Otherwise, Si will be depleted in the boundary layer. This explains why Si is enriched in the {−111} sectors in this study (crystal #5 in Fig. 5a), but in the {$hk0$} sectors in the case of Hawaii (Hammer et al., 2016; Welsch et al., 2016), because SiO_2 contents of clinopyroxenes are higher in the Hawaiian melts (Hammer et al., 2016), but are lower than those in the Sailipu melts. The {$hk0$} sectors in the sector-zoned crystals formed in this scenario are closer to equilibrium (Fig. 8a–b). It is worth noting that the formation of sector-zoned clinopyroxenes at high degrees of undercooling violates the classic descriptions of sector zoning, which emphasize that different sectors grew simultaneously (e.g., Reeder and Paquette, 1989). However, textural and compositional differences within these crystals occur among different crystallographic directions, consistent with the observation of sector zoning. In addition, the irregular, bright domains within the {−111} sectors (Fig. 3g) are traditionally interpreted as intrasectoral zoning (Paquette and Reeder, 1990), whereas they represent dendrites forming at the early stage of clinopyroxene growth in this study. Application of the regression model of Masotta et al. (2020) to estimate the degree of undercooling demonstrates that the reversed sector zoning (crystal #5) crystallized at higher degrees of undercooling ($\Delta T = {\sim}62 \pm 22\,°C$) than those of the normal sector zoning (crystal #4; $\Delta T = {\sim}54 \pm 22\,°C$) in the same sample. In addition, the average crystallization pressure of crystal #4 (449 MPa) is higher than it of crystal #5 (399 MPa), suggesting that high degrees of undercooling were achieved by rapid magma decompression and degassing.

5.3. Implications for magma dynamics

Disequilibrium crystal growth can compromise pressure estimates using clinopyroxene. For example, different domains within sector-zoned clinopyroxene have obvious differences in composi-
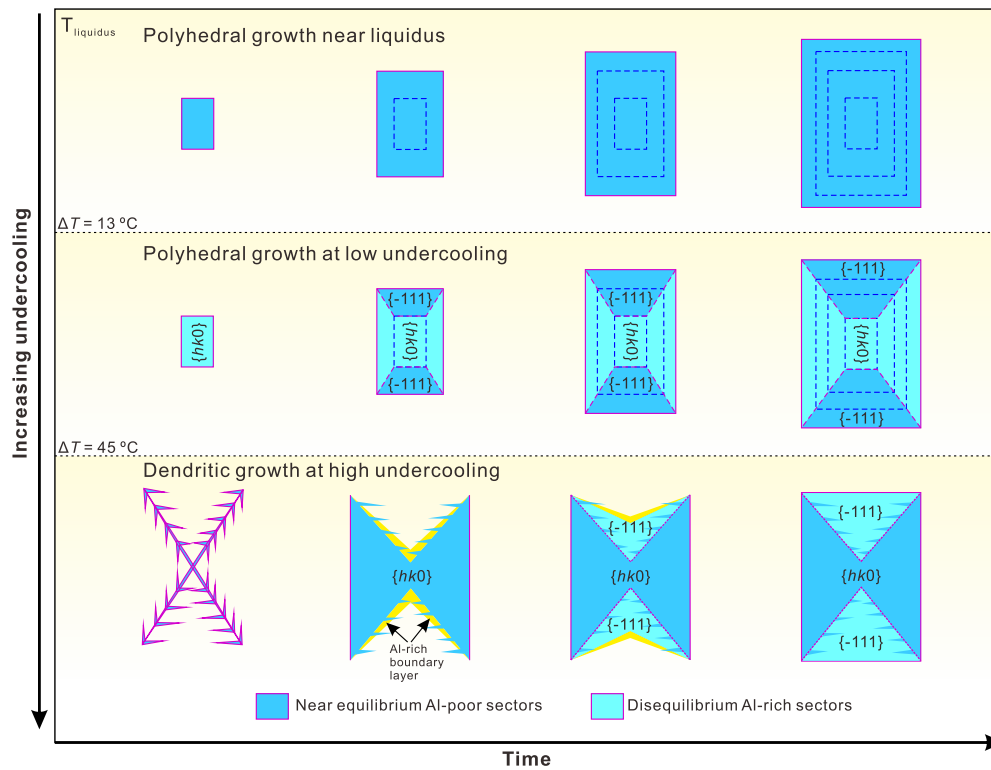
Fig. 9. Crystal growth mechanisms of clinopyroxene at different degrees of undercooling. Near-liquidus crystallization produces concentrically zoned crystals. At $\Delta T =$ 13–45 °C, all crystal faces grow concurrently, and concentric zones cut through the sector zone boundaries. In this case, growth rates of {−111} sectors are faster than those of {hk0} sectors. Sector-zoned clinopyroxenes formed by this process have Si–Mg-rich {−111} and Al-Ti-rich {hk0} sectors, and the {−111} sectors are closer to equilibrium. At $\Delta T > 45$ °C, the prism sectors {hk0} initially form by dendritic growth, followed by backfill on {−111} sectors. Early dendritic growth and ripening at high ΔT generates hopper crystals (i.e., {hk0} sectors). These hopper crystals have V-shaped cavities (i.e., {−111} sectors), in which there is a crystal-melt boundary layer with high Al contents (Masotta et al., 2020), and thus the crystal domains formed in V-shaped cavities ({−111} sectors) are characterized by high Al contents. The behavior of other cations is complex, and the distribution of these cations amongst the {−111} and {hk0} sectors is variable. The {hk0} sectors in the sector-zoned crystals formed in this scenario are closer to equilibrium. The crystal growth kinetics at different degrees of undercooling are consistent with the integrated approach of experimental and theoretical results by Giuliani et al. (2020), but the growth mechanism of sector-zoned clinopyroxenes at high degrees of undercooling is new.

tions (Fig. 5), which can lead to spurious geobarometric results (Fig. 8d). It is difficult to identify which domain (or sector) records reliable information using the existing equilibrium tests (Fig. 8). Our results suggest that Al_2O_3 is a robust indicator of equilibrium. Al_2O_3-poor sectors likely record relatively true equilibrium compositions, rather than specific crystal faces (e.g., {−111} or {hk0} sectors), because growth processes of sector-zoned crystals are different at high and low degrees of undercooling (Fig. 9). The suggestion that Al_2O_3-poor sectors are closer to equilibrium is consistent with the study of Hammer et al. (2016). This should help guide thermobarometric calculations on natural samples, particularly for spatially heterogeneous sector-zoned clinopyroxenes.

Apatite inclusions are abundant in most Sailipu clinopyroxene crystals (Fig. 3; Supplementary Fig. S2), as observed in other alkaline igneous systems (e.g., Ubide et al., 2019b). Interestingly, most apatites are distributed along concentric growth bands (Fig. 3; Supplementary Fig. S2). Traditionally, the crystallization of mineral inclusions is thought to happen earlier than the host crystal, indicating apatite crystallization before clinopyroxene. However, it is inconsistent with the fact that the saturation of apatite in mafic melts generally occurs at the late stages of crystallization (Tollari et al., 2006). To better understand the origin of the apatite inclusions, we explored the behavior of P in the crystal–melt diffusive boundary layer during clinopyroxene growth. A diffusive crystal growth model (Zhang, 2008; Chen and Zhang, 2009) was used to undertake numerical modeling. The stability of clinopyroxene in mafic magmas is controlled mainly by CaO and MgO diffusion in the melt (Chen and Zhang, 2009). Given that the CaO content is higher than

MgO in clinopyroxene, we used CaO to track the crystal growth rates, for the sake of simplicity during mathematic approach. Based on the interface-fixed reference frame described by Zhang (2008), concentration profiles of P in melts adjacent to growing crystals can be expressed by the one-dimensional diffusive equation:

$$\frac{\partial C_P}{\partial t} = D_P \frac{\partial^2 C_P}{\partial x^2} + \alpha \sqrt{D_{CaO}/t} \frac{\partial C_P}{\partial x}. \tag{1}$$

This diffusive equation can be solved by the Boltzmann transformation, resulting in a solution for C_P of:

$$C_P = C_P^\infty + (C_P^0 - C_P^\infty)\text{erfc}(\frac{x}{\sqrt{4D_P t}} + \alpha\sqrt{D_{CaO}/D_P})$$
$$/\text{erfc}\left(\alpha\sqrt{D_{CaO}/D_P}\right). \tag{2}$$

With C_P^0 being calculated as:

$$C_P^0 = C_P^\infty/[1 + \sqrt{\pi}(\alpha\sqrt{D_{CaO}/D_P})e^{(\alpha\sqrt{D_{CaO}/D_P})^2}$$
$$\times \text{erfc}(\alpha\sqrt{D_{CaO}/D_P})(K_P - 1)], \tag{3}$$

where C_P = concentration of P in the diffusive boundary layer, t = time, x = distance from the crystal–melt interface, D_{CaO} = diffusivity of CaO in the melt, C_P^∞ = concentration of P in the far-field melt, C_P^0 = concentration of P in the melt at the crystal–melt interface, D_P = diffusivity of P in the melt, α = empirical parameter related to the growth rate, K_P = clinopyroxene/melt partition coefficient for P, and erfc = complementary error function. The crystal growth rate (u) can be expressed as
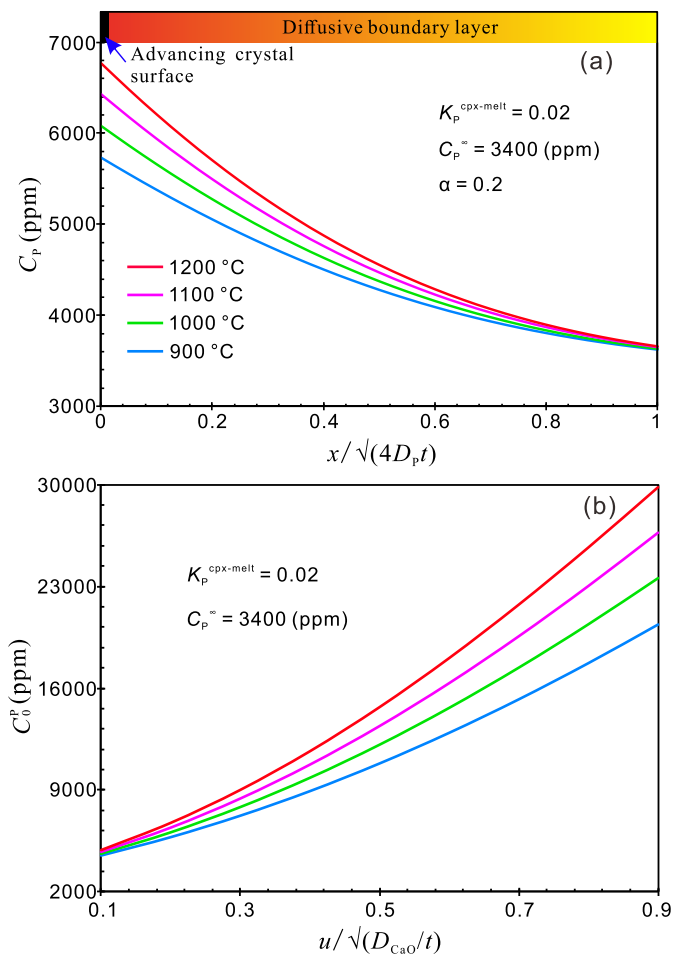
Fig. 10. The behavior of P in the crystal–melt diffusive boundary layer during clinopyroxene growth. (a) Diffusion profiles of P in the boundary layer, using Equation (2). (b) Relationship between P concentrations in the interface melt and growth rates, using Equation (3). The clinopyroxene/melt partition coefficient for P ($K_P^{cpx-melt} = 0.02$) is from Baziotis et al. (2019). Whole-rock P concentrations were assumed as the P concentrations in far-field melt ($C_P^{\infty} = 3400$ ppm). Calculated results using $\alpha = 0.2$ are shown in (a).

$\alpha(D_{CaO}/t)^{1/2}$ (Zhang, 2008). Temperature-dependent diffusivities were used: $\ln D_{CaO} = -10.517 - 21205/T$ (Chen and Zhang, 2009); $D_P = -6.3\exp(-147000/RT)$ (Watson et al., 2015); T is temperature in Kelvin and R is the gas constant. The results are shown in Fig. 10 and two key observations can be drawn. The first is that P concentrations in melt increase from the far-field melt towards the crystal–melt interface, and can be highly concentrated in the melt near the interface (Fig. 10a). The second is that P concentrations in the interface melt increase with increasing crystal growth rate (Fig. 10b). Thus, apatite inclusions in the Sailipu clinopyroxenes are a result of phosphate saturation in the crystal–melt diffusive boundary layer. Furthermore, the apatite inclusions in clinopyroxene suggest rapid crystal growth, because P will be significantly concentrated in the interface melt at high crystal growth rates (Fig. 10b).

Complex crystal textures are commonly regarded as being evidence of magma mixing or recharge, such as embayed, sieved, or patchily zoned crystals. However, these crystal textures can also be attributed to disequilibrium crystal growth at high degrees of undercooling, when early dendritic growth is followed by incomplete infilling (e.g., Fig. 3d, e, f, h), possibly without magma replenishment. In addition, Cr is a highly compatible trace element in clinopyroxene and can have important implications for magmatic processes. Although no obvious Cr zoning has been observed in

different clinopyroxene sectors from some typical alkaline igneous systems, such as Mt. Etna (Sicily, Italy; Ubide et al., 2019a), sector-zoned clinopyroxene crystals in this study exhibit clear Cr zoning amongst different sectors. The {−111} sectors have lower Cr concentrations than the {hk0} sectors. This means that clinopyroxene Cr concentrations are also affected by crystallographic controls, and not just the melt composition.

6. Conclusions

On the basis of detailed textural and compositional analysis of a large number of clinopyroxene crystals from the Sailipu alkaline volcanic field, we suggest that sector-zoned clinopyroxenes are formed by two different processes at high and low degrees of undercooling. At low degrees of undercooling, all crystal faces grow concurrently. These clinopyroxenes generally have Si–Mg-rich {−111} sectors and Al–Ti-rich {hk0} sectors, with the {−111} sectors being closer to equilibrium. At high degrees of undercooling, the prism {hk0} sectors initially form by dendritic growth, and followed by backfill on Al-rich {−111} sectors. The {hk0} sectors in the sector-zoned crystals formed by this process are closer to equilibrium. The formation of sector-zoned clinopyroxenes at high degrees of undercooling violates the classic descriptions of sector and intrasectoral zoning, but all of them show crystallographically controlled zoning patterns. We emphasize that Al_2O_3 is a robust indicator of equilibrium, and that Al_2O_3-poor sectors record closest to equilibrium compositions, rather than specific crystal faces. The distribution of other cations is variable. Our results will allow better application of clinopyroxene-related geothermobarometers. We also found that apatite inclusions in clinopyroxene can reflect rapid crystal growth. These results may contribute to the improved use of clinopyroxene as an archive of processes in magmatic plumbing systems. It is noteworthy that the crystal growth mechanism for clinopyroxene at high undercooling being suggested in this study is based on textural and major element analyses, and further research using experimental approach is highly desirable.

Appendix A. Supplementary material

Supplementary material related to this article can be found online at https://doi.org/10.1016/j.epsl.2021.117005.

References

Baziotis, I., Xydous, S., Asimow, P.D., Mavrogonatos, C., Berndt, J., 2019. The potential of phosphorus in clinopyroxene as a geospeedometer: examples from mantle xenoliths. Geochim. Cosmochim. Acta 266, 307–331. https://doi.org/10.1016/j.gca.2019.04.024.

Blundy, J.D., Falloon, T.J., Wood, B.J., Dalton, J.A., 1995. Sodium partitioning between clinopyroxene and silicate melts. J. Geophys. Res., Solid Earth 100, 15501–15515. https://doi.org/10.1029/95JB00954.

Chen, Y., Zhang, Y., 2009. Clinopyroxene dissolution in basaltic melt. Geochim. Cosmochim. Acta 73, 5730–5747. https://doi.org/10.1016/j.gca.2009.06.016.

Costa, F., Shea, T., Ubide, T., 2020. Diffusion chronometry and the timescales of magmatic processes. Nat. Rev. Earth Environ. 1, 201–214. https://doi.org/10.1038/s43017-020-0038-x.

Downes, M.J., 1974. Sector and oscillatory zoning in calcic augites from M. Etna, Sicily. Contrib. Mineral. Petrol. 47, 187–196. https://doi.org/10.1007/BF00371538.

Dowty, E., 1976. Crystal structure and crystal growth: II. Sector zoning in minerals. Am. Mineral. 61, 460–469.

Faure, F., Schiano, P., Trolliard, G., Nicollet, C., Soulestin, B., 2007. Textural evolution of polyhedral olivine experiencing rapid cooling rates. Contrib. Mineral. Petrol. 153, 405–416. https://doi.org/10.1007/s00410-006-0154-8.

Giuliani, L., Iezzi, G., Mollo, S., 2020. Dynamics of volcanic systems: physical and chemical models applied to equilibrium versus disequilibrium solidification of magmas. In: Vetere, F. (Ed.), Dynamic Magma Evolution. In: Geophysical Monograph Series, vol. 254. John Wiley & Sons Inc., New Jersey, USA. ISBN 9781119521136, pp. 101–132, 206 pp.

Guo, Z., Wilson, M., 2019. Late Oligocene–early Miocene transformation of post-collisional magmatism in Tibet. Geology 47, 776–780. https://doi.org/10.1130/G46147.1.

Guo, Z., Wilson, M., Zhang, M., Cheng, Z., Zhang, L., 2015. Post-collisional ultrapotassic mafic magmatism in South Tibet: products of partial melting of pyroxenite in the mantle wedge induced by roll-back and delamination of the subducted Indian continental lithosphere slab. J. Petrol. 56, 1365–1406. https://doi.org/10.1093/petrology/egv040.

Hammer, J.E., 2008. Experimental studies of the kinetics and energetics of magma crystallization. Rev. Mineral. Geochem. 69, 9–59. https://doi.org/10.2138/rmg.2008.69.2.

Hammer, J.E., Jacob, S.R., Welsch, B., Hellebrand, E., Sinton, J.M., 2016. Clinopyroxene in postshield Haleakala ankaramite: 1. Efficacy of thermobarometry. Contrib. Mineral. Petrol. 171, 7. https://doi.org/10.1007/s00410-015-1212-x.

Herring, C., 1951. Some theorems on the free energies of crystal surfaces. Phys. Rev. 82, 87–93. https://doi.org/10.1103/PhysRev.82.87.

Hollister, L.S., Gancarz, A.J., 1971. Compositional sectorzoning in clinopyroxene from the Narce area, Italy. Am. Mineral. 56, 959–979.

Kirkpatrick, R.J., Kuo, L., Melchior, J., 1981. Crystal growth in incongruently-melting compositions: programmed cooling experiments with diopside. Am. Mineral., 223–241.

Kouchi, A., Sugawara, Y., Kashima, K., Sunagawa, I., 1983. Laboratory growth of sector zoned clinopyroxenes in the system CaMgSi$_2$O$_6$–CaTiAl$_2$O$_6$. Contrib. Mineral. Petrol. 83, 177–184. https://doi.org/10.1007/BF00373091.

Leung, I.S., 1974. Sector-zoned titanaugites: morphology, crystal chemistry, and growth. Am. Mineral. 59, 127–138.

Liu, D., Zhao, Z., Zhu, D.-C., Niu, Y., DePaolo, D.J., Harrison, T.M., Mo, X., Dong, G., Zhou, S., Sun, C., Zhang, Z., Liu, J., 2014. Postcollisional potassic and ultrapotassic rocks in southern Tibet: mantle and crustal origins in response to India–Asia collision and convergence. Geochim. Cosmochim. Acta 143, 207–231. https://doi.org/10.1016/j.gca.2014.03.031.

Lofgren, G.E., Huss, G.R., Wasserburg, G.J., 2006. An experimental study of trace-element partitioning between Ti-Al-clinopyroxene and melt: equilibrium and kinetic effects including sector zoning. Am. Mineral. 91, 1596–1606. https://doi.org/10.2138/am.2006.2108.

Masotta, M., Pontesilli, A., Mollo, S., Armienti, P., Ubide, T., Nazzari, M., Scarlato, P., 2020. The role of undercooling during clinopyroxene growth in trachybasaltic magmas: insights on magma decompression and cooling at Mt. Etna volcano. Geochim. Cosmochim. Acta 268, 258–276. https://doi.org/10.1016/j.gca.2019.10.009.

Mollo, S., Hammer, J.E., 2017. Dynamic crystallization in magmas. EMU Notes Mineral. 16, 373–418. https://doi.org/10.1180/EMU-notes.16.12.

Mollo, S., Blundy, J., Scarlato, P., De Cristofaro, S.P., Tecchiato, V., Di Stefano, F., Vetere, F., Holtz, F., Bachmann, O., 2018. An integrated P-T-H$_2$O-lattice strain model to quantify the role of clinopyroxene fractionation on REE+Y and HFSE patterns of mafic alkaline magmas: application to eruptions at Mt. Etna. Earth-Sci. Rev. 185, 32–56. https://doi.org/10.1016/j.earscirev.2018.05.014.

Mollo, S., Gaudio, P.D., Ventura, G., Iezzi, G., Scarlato, P., 2010. Dependence of clinopyroxene composition on cooling rate in basaltic magmas: implications for thermobarometry. Lithos 118, 302–312. https://doi.org/10.1016/j.lithos.2010.05.006.

Mollo, S., Putirka, K.D., Misiti, V., Soligo, M., Scarlato, P., 2013. A new test for equilibrium based on clinopyroxene-melt pairs: clues on the solidification temperatures of Etnean alkaline melts at post-eruptive conditions. Chem. Geol. 352, 92–100. https://doi.org/10.1016/j.chemgeo.2013.05.026.

Nakamura, Y., 1973. Origin of sector-zoning of igneous clinopyroxenes. Am. Mineral. 58, 986–990.

Neave, D.A., Putirka, K., 2017. A new clinopyroxene-liquid barometer, and implications for magma storage pressures under Icelandic rift zones. Am. Mineral. 102, 777–794. https://doi.org/10.2138/am-2017-5968.

Neave, D.A., Bali, E., Guðfinnsson, G.H., Halldorsson, S.A., Kahl, M., Schmidt, A., Holtz, F., 2019. Clinopyroxene–liquid equilibria and geothermobarometry in natural and experimental tholeiites: the 2014–2015 Holuhraun eruption, Iceland. J. Petrol. 60, 1653–1680. https://doi.org/10.1093/petrology/egz042.

Ni, H., Keppler, H., Walte, N.P., Schiavi, F., Chen, Y., Masotta, M., Li, Z., 2014. In situ observation of crystal growth in a basalt melt and the development of crystal size distribution in igneous rocks. Contrib. Mineral. Petrol. 167, 1003. https://doi.org/10.1007/s00410-014-1003-9.

Paquette, J., Reeder, R.J., 1990. New type of compositional zoning in calcite: insights into crystal-growth mechanisms. Geology 18, 1244–1247. https://doi.org/10.1130/0091-7613(1990)018<1244:NTOCZI>2.3.CO;2.

Perinelli, C., Mollo, S., Gaeta, M., De Cristofaro, S.P., Palladino, D.M., Armienti, P., Scarlato, P., Putirka, K.D., 2016. An improved clinopyroxene-based hygrometer for Etnean magmas and implications for eruption triggering mechanisms. Am. Mineral. 101, 2774–2777. https://doi.org/10.2138/am-2016-5916.

Pontesilli, A., Masotta, M., Nazzari, M., Mollo, S., Armienti, P., Scarlato, P., Brenna, M., 2019. Crystallization kinetics of clinopyroxene and titanomagnetite growing from a trachybasaltic melt: new insights from isothermal time-series experiments. Chem. Geol. 510, 113–129. https://doi.org/10.1016/j.chemgeo.2019.02.015.

Putirka, K., 2008. Thermometers and barometers for volcanic systems. Rev. Mineral. Geochem. 69, 61–120. https://doi.org/10.2138/rmg.2008.69.3.

Putirka, K., 2017. Down the crater: where magmas are stored and why they erupt. Elements 13, 11–16. https://doi.org/10.2113/gselements.13.1.11.

Reeder, R.J., Paquette, J., 1989. Sector zoning in natural and synthetic calcites. Sediment. Geol. 65, 239–247. https://doi.org/10.1016/0037-0738(89)90026-2.

Schwandt, C.S., McKay, G.A., 2006. Minor- and trace-element sector zoning in synthetic enstatite. Am. Mineral. 91, 1607–1615. https://doi.org/10.2138/am.2006.2093.

Shea, T., Hammer, J.E., Hellebrand, E., Mourey, A.J., Costa, F., First, E.C., Lynn, K.J., Melnik, O.E., 2019. Phosphorus and aluminum zoning in olivine: contrasting behavior of two nominally incompatible trace elements. Contrib. Mineral. Petrol. 174, 95. https://doi.org/10.1007/s00410-019-1639-6.

Shimizu, N., 1981. Trace element incorporation into growing augite phenocryst. Nature 289, 575–577. https://doi.org/10.1038/289575a0.

Tollari, N., Toplis, M.J., Barnes, S.J., 2006. Predicting phosphate saturation in silicate magmas: an experimental study of the effects of melt composition and temperature. Geochim. Cosmochim. Acta 70, 1518–1536. https://doi.org/10.1016/j.gca.2005.11.024.

Ubide, T., Caulfield, J., Brandt, C., Bussweiler, Y., Mollo, S., Di Stefano, F., Nazzari, M., Scarlato, P., 2019b. Deep magma storage revealed by multi-method elemental mapping of clinopyroxene megacrysts at Stromboli volcano. Front. Earth Sci. 7, 239. https://doi.org/10.3389/feart.2019.00239.

Ubide, T., Mollo, S., Zhao, J.-X., Nazzari, M., Scarlato, P., 2019a. Sector-zoned clinopyroxene as a recorder of magma history, eruption triggers, and ascent rates. Geochim. Cosmochim. Acta 251, 265–283. https://doi.org/10.1016/j.gca.2019.02.021.

Watson, E.B., Liang, Y., 1995. A simple model for sector zoning in slowly grown crystals: implications for growth rate and lattice diffusion, with emphasis on accessory minerals in crustal rocks. Am. Mineral. 80, 1179–1187. https://doi.org/10.2138/am-1995-11-1209.

Watson, E.B., Cherniak, D., Holycross, M., 2015. Diffusion of phosphorus in olivine and molten basalt. Am. Mineral. 100, 2053–2065. https://doi.org/10.2138/am-2015-5416.

Welsch, B., Faure, F., Famin, V., Baronnet, A., Bachelery, P., 2013. Dendritic crystallization: a single process for all the textures of olivine in basalts? J. Petrol. 54, 539–574. https://doi.org/10.1093/petrology/egs077.

Welsch, B., Hammer, J.E., Hellebrand, E., 2014. Phosphorus zoning reveals dendritic architecture of olivine. Geology 42, 867–870. https://doi.org/10.1130/G35691.1.

Welsch, B., Hammer, J.E., Baronnet, A., Jacob, S.R., Hellebrand, E., Sinton, J.M., 2016. Clinopyroxene in postshield Haleakala ankaramite: 2. Texture, compositional zoning and supersaturation in the magma. Contrib. Mineral. Petrol. 171, 6. https://doi.org/10.1007/s00410-015-1213-9.

Xing, C.-M., Wang, C.-Y., Tan, W., 2017. Disequilibrium growth of olivine in mafic magmas revealed by phosphorus zoning patterns of olivine from mafic-ultramafic intrusions. Earth Planet. Sci. Lett. 479, 108–119. https://doi.org/10.1016/j.epsl.2017.09.005.

Zhang, Y., 2008. Geochemical Kinetics. Princeton University Press, Princeton, 631 p.

Zhang, Y., Ni, H., Chen, Y., 2010. Diffusion data in silicate melts. Rev. Mineral. Geochem. 72, 311–408. https://doi.org/10.2138/rmg.2010.72.8.

Zhao, Z., Mo, X., Dilek, Y., Niu, Y., DePaolo, D.J., Robinson, P., Zhu, D.-C., Sun, C., Dong, G., Zhou, S., 2009. Geochemical and Sr–Nd–Pb–O isotopic compositions of the post-collisional ultrapotassic magmatism in SW Tibet: petrogenesis and implications for India intra-continental subduction beneath southern Tibet. Lithos 113, 190–212. https://doi.org/10.1016/j.lithos.2009.02.004.

Zhou, J.-S., Yang, Z.-S., Wang, Q., Zheng, Y.-C., Hou, Z.-Q., Wyman, D.A., 2020. Extraction of high-silica granites from an upper crustal magma reservoir: insights from the Narusongduo magmatic system, Gangdese arc. Am. Mineral. 105, 1572–1584. https://doi.org/10.2138/am-2020-7369.